

Article

Trace and Rare Earth Elements, and Sr Isotopic Compositions of Fluorite from the Shihuiyao Rare Metal Deposit, Inner Mongolia: Implication for Its Origin

Zhen-Peng Duan ¹, Shao-Yong Jiang ^{1,*}, Hui-Min Su ¹, Xin-You Zhu ², Tao Zou ² and Xi-Yin Cheng ²

¹ State Key Laboratory of Geological Processes and Mineral Resources, Collaborative Innovation Center for Exploration of Strategic Mineral Resources, School of Earth Resources, China University of Geosciences, Wuhan 430074, China; dzp8697@126.com (Z.-P.D.); suhm@cug.edu.cn (H.-M.S.)

² Beijing Institute of Geology for Mineral Resources, Beijing 100012, China; zhuxinyou@outlook.com (X.-Y.Z.); 13436751833@163.com (T.Z.); chengxiyin36@126.com (X.-Y.C.)

* Correspondence: shyjiang@cug.edu.cn

Received: 29 August 2020; Accepted: 2 October 2020; Published: 4 October 2020



Abstract: Abundant fluorites occur in the Shihuiyao rare metal (Nb-Ta-Rb) deposit in Inner Mongolia of NE China, and they can be classified by their occurrence into three types. Type I occurs disseminated in greisen pockets of albitized granite. Type II occurs in the skarn zone between granite and carbonate host rocks, and it can be subdivided into different subtypes according to color, namely dark purple (II-D), magenta (II-M), green (II-G), light purple (II-P), and white (II-W). Type III are the fluorite-bearing veins in the silty mudstones. On the basis of petrography of the fluorites and their high contents of HFSEs (high field strength elements) and LILEs (large ion lithophile elements), strong negative Eu anomalies, and tetrad effects, we suggest that Type I fluorites crystallized in a late-magmatic stage with all the components derived from the granite. The high Y/Ho ratios suggest that the Type II fluorites crystallized in the early- or late-hydrothermal stage. The rare earth elements (REEs) characterized by various Eu anomalies of the Type II fluorites indicate a mixed origin for ore-forming metals from granite-related fluids and limestones, and the oxygen fugacity increased during fluid migration and cooling. Compared to the Type II fluorites, the similar trace element contents of the Type III suggest a similar origin, and remarkable positive Eu anomalies represent a more oxidizing environment. The Sr isotopic composition ($^{87}\text{Sr}/^{86}\text{Sr}$)_i = 0.710861) of the Type I fluorites may represent that of the granite-derived fluids, whereas the ($^{87}\text{Sr}/^{86}\text{Sr}$)_i ratios of the Type II (0.710168–0.710380) and Type III (0.709018) fluorites are lower than that of the Type I fluorites but higher than those of the Late Permian–Early Triassic seawater, suggesting a binary mixed Sr source, i.e., granite-derived fluids and marine limestones. Nevertheless, the proportion of limestone-derived Sr in the mixture forming the Type III fluorites is much higher than that of Type II. The rare metal Nb and Ta get into the granite-derived F-rich fluids by complexing with F and precipitate in the form of columbite-group minerals after the Type I fluorites crystallize. Most of Nb and Ta may have deposited as columbite-group minerals during the magmatic stage, resulting in no Nb-Ta mineralization in the hydrothermal stage when the Type II and III fluorites formed. Hence, the Type I fluorites in the Shihuiyao mining area can be used as an important exploration tool for the Nb-Ta mineralization.

Keywords: fluorite; fluid evolution; Sr source; Shihuiyao rare metal deposit; Inner Mongolia

1. Introduction

Fluorite and its trace element geochemical features have been studied by many researchers in an attempt to understand the geological conditions that occurred during the formation of fluorite and associated mineralization [1–9]. Fluorite is one of the most common hydrothermal minerals in many deposits, which has relatively high rare earth element (REE) contents. Therefore, the REE concentrations of fluorite occurring in different stages can provide insights into the element behavior and the evolution of a hydrothermal fluid [1–3,5,7,8,10,11]. In addition, because Rb is much less compatible than Sr in fluorite, fluorite will possess a very low Rb/Sr ratio, permitting the determination of $^{87}\text{Sr}/^{86}\text{Sr}$ ratio of fluids from which fluorite precipitated [10,12–15].

The Southern Great Xing'an Range (SGXR) is one of the most important polymetallic metallogenic belts in China, and it also contains a large number of fluorite occurrences [9]. Shihuiyao was recently discovered as a giant Nb-Ta-Rb rare metal deposit in XilinHot, Inner Mongolia. Previous studies have mainly focused on the petrology, age, and genesis of the Nb-Ta-Rb deposits [16–18]. This deposit may be an integrated product of the crystallization of granitic magma in the early stage and hydrothermal metasomatic interaction later, of which the latter includes the main metallogenic stages of Nb, Ta, and Rb [18]. The ore bodies mainly occur in albitized and greisenized granites. The Nb-Ta minerals disseminated in the albitized granites mainly include manganocolumbite, columbite–tantalite, columbite–manganotantalite, wodginite, microlite, and the Rb minerals are mainly mica and amazonite [16–18]. Since fluorite is widespread in the Shihuiyao area in a close association with the rare metal mineralization, its chemical and isotopic characteristics can shed new light on its origin and associated rare metal mineralization. Hence, we focused on the trace and rare earth element concentrations, as well as on Sr isotope compositions of various types of fluorites from the Shihuiyao rare metal mining area, aiming to investigate the origin and water–rock interaction during the formation of fluorite and associated rare metal mineralization.

2. Geological Setting and Mineralization

The Shihuiyao Nb-Ta-Rb rare metal deposit is located in the SGXR, which belongs to the Xing'an–Mongolian Orogenic Belt (XMOB). The XMOB is the eastern segment of the Central Asian Orogenic Belt (CAOB), and it is tectonically located in the area surrounded by the Siberian Craton to the north, the North China Craton (NCC) to the south, and the western Pacific Plate to the east (Figure 1a). The eastern segment of the CAOB consists of four blocks, namely, the Erguna Block (EB), the Xing'an Block (XB), the Jiamusi Block (JB), and the Songliao–Xilinhote Block (SXB), and four sutures, including the Xinlin–Xiguitu suture (XXS), the Heihe–Hegenshan suture (HHS), the Mudanjiang–Yilan suture (MYS) and the Solonker–Xar Moron suture (SXS) ([19]). The study area is situated on the southwestern part of the SXB and lies between the HHS and the western part of SXS (Figure 1a).

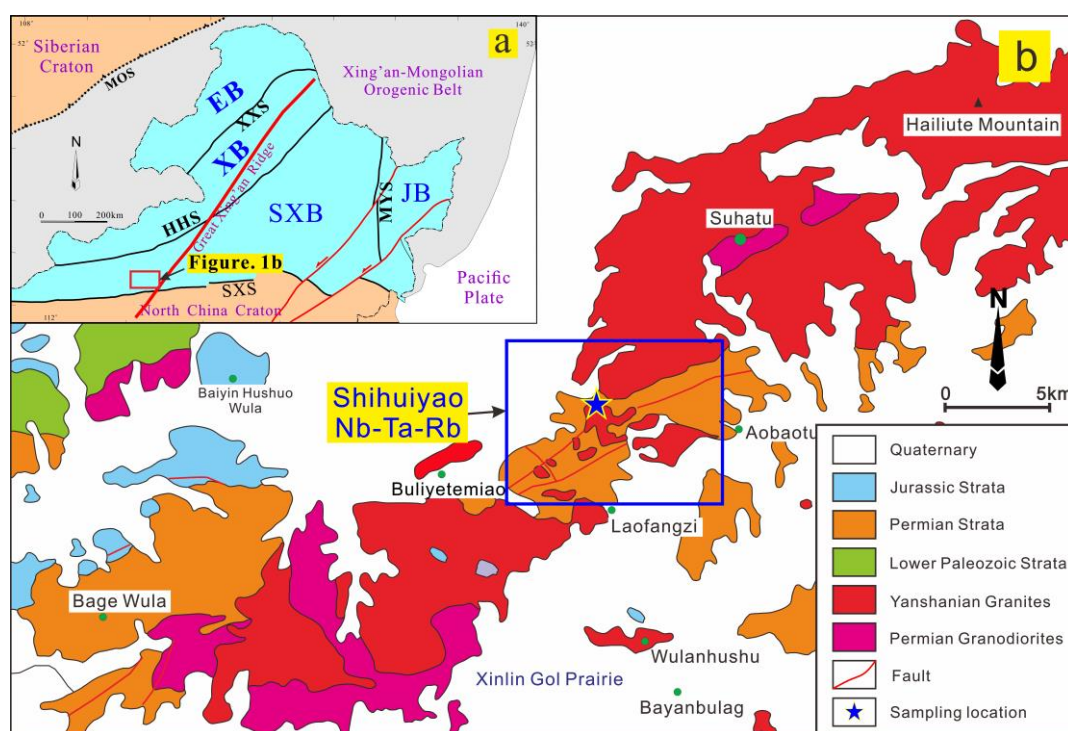


Figure 1. (a) Location map of the Shihuiyao deposit in Inner Mongolia (modified from [19]); (b) Simplified geological setting of the Shihuiyao deposit (modified from [18]). EB—Erguna block, XB—Xing’an block, SXB—Songliao–Xilinhot block, JB—Jiamusi block; MOS—Mongol–Okhotsk suture, XXS—Xinlin–Xiguitu suture, HHS—Heihe–Hegenshan suture, MYS—Mudanjiang–Yilan suture, SXS—Solonker–Xar Moron suture.

The igneous rocks distributed along a NE trend in the area are mainly Permian granodiorites and Yanshanian granites (Figure 1b), which are thought to be controlled by the closure of the Paleo-Asian Ocean (300–260 Ma) and the subduction of the Paleo-Pacific plate (150–120 Ma), respectively [19–21]. The regional basement includes the Lower Paleozoic Xilin Gol Complex, Permian strata (Dashizhai, Zhesi, and Linxi formations), and Jurassic strata (Manketouebo Formation), (Figure 1b). The Shihuiyao mining area is constituted by Yanshanian granites, Late Permian–Early Triassic Linxi Formation, and Quaternary. The Linxi Formation, whose depositional age is from Late Permian to Early Triassic [22], mainly consists of mudstone, siltstone or calcareous siltstone, sandstone or calcareous sandstone, and slate, with lesser amounts of limestone beds and lenses [23].

In the northwestern part of the Shihuiyao mining area, the fluorite mineralization mainly occurs in the skarn zone between the albitized granite and wall rocks of the Linxi Formation, followed by disseminated mineralization in greisen pockets and fluorite-bearing veins in wall rocks. Fluorite mineralization in the skarn zone mainly occurs as veins, with various colors of dark or light purple, magenta, white, and green. The veins generally consist of banded fluorite interlayered with calcite and chalcedony.

The main rock types of the wall rocks are limestones and silty mudstones. The alteration of the wall rocks is mainly characterized by skarnization and silicification. The albitized granite (A–G) is composed of quartz (≈ 35 vol%), albite (≈ 25 vol%), K-feldspar (≈ 35 vol%), muscovite (≈ 5 vol%), and minor columbite-group minerals (less than 2 vol%), with zircon and monazite as the main accessory minerals (Figure 2a,b). Albite clearly replaced K-feldspar and muscovite (Figure 2b). In addition, the greisen pockets are distributed randomly in the granite, with a size of several centimeters to tens of centimeters in diameter. Sun et al. [17] obtained a muscovite ^{40}Ar - ^{39}Ar age of 144.7 ± 1.1 Ma from the greisen in the albitized granite.

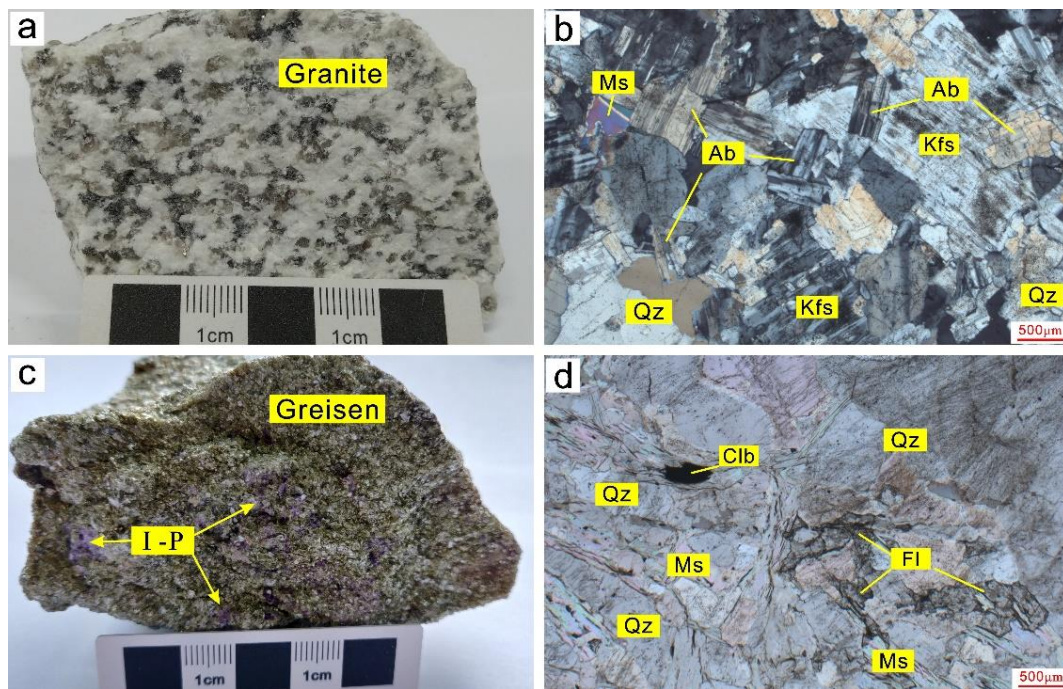


Figure 2. (a,b) Hand specimen and photomicrograph of the albitized granite; (c,d) Hand specimen and photomicrograph of the fluorite-bearing greisen (Type I). Ab—albite, Fl—Fluorite, Kfs—K-feldspar, Ms—muscovite, Qz—quartz, Clb—columbite.

3. Samples and Analytical Methods

3.1. Samples

Fifteen fluorite samples and one fresh albitized granite sample were collected from the Shihuiyao fluorite mineralization area. The types of fluorite were identified by their occurrences. Type I: purple fluorite (I-P) from the greisen in the albitized granites (Figure 2c,d); Type II: fluorites of various colors from the skarn zone: dark purple fluorite (II-D) (Figure 3a,b), magenta fluorite (II-M) (Figure 3a,b), green fluorite (II-G) (Figure 3c,d), light purple fluorite (II-P) (Figure 3c,d), and white fluorite (II-W) (Figure 4a,b); Type III purple fluorite (III-P) from the veins in the silty mudstones (Figure 4c,d), and the veins mainly consist of albite (altered), quartz, and fluorite (Figure 4d). We can observe some columbite-group minerals associated with mica in greisen pockets (Figure 2d), whereas there is no Nb-Ta mineralization in the skarn zone or veins where the Type II and III fluorites precipitated, respectively.

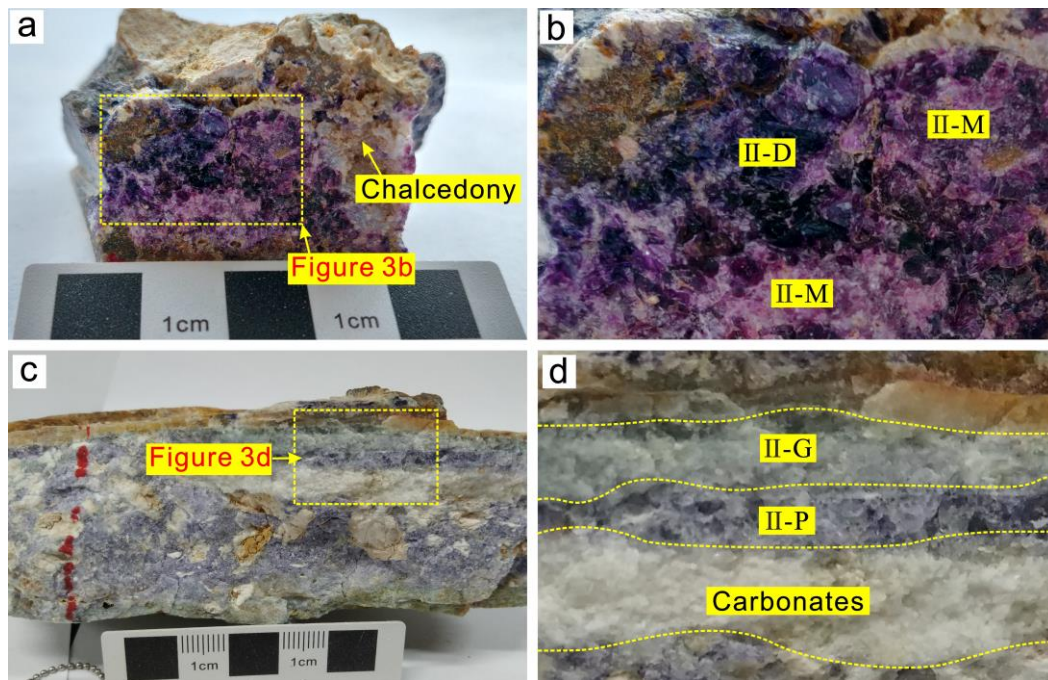


Figure 3. (a,b) Hand specimen of dark purple and magenta fluorites in the skarn zone (Type II); (c,d) Hand specimen of green and purple fluorites in the skarn zone (Type II).

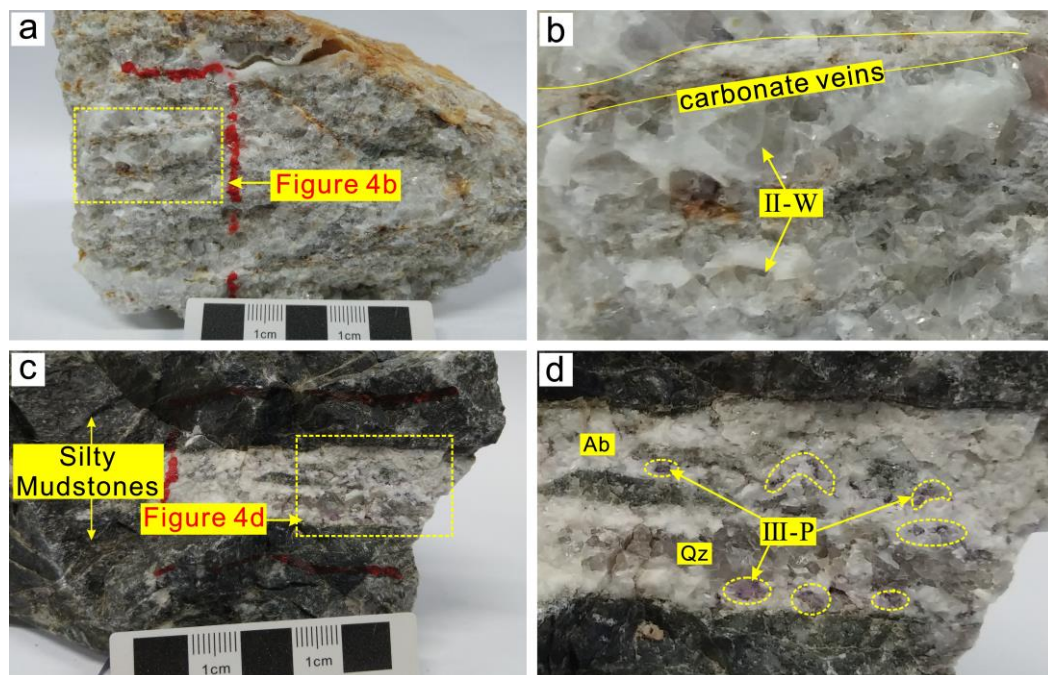


Figure 4. (a,b) Hand specimen of white fluorites in the skarn zone (Type II); (c,d) Hand specimen of fluorite-bearing veins in silty mudstones (Type III). Ab—albite, Qz—quartz.

3.2. Whole-Rock Trace-Elements Analyses

The albitized granite samples for whole-rock geochemical analyses were crushed to fine powders of 200-mesh through an agate mill. Trace element contents were determined by a Finnigan MAT Element II high-resolution inductively coupled plasma mass spectrometry (HR-ICP-MS) at State Key Laboratory for Mineral Deposits Research, Nanjing University, Nanjing, China. The analytical conditions and procedures are similar to those described in the paper of Gao et al. [24]. About 50 mg of

powdered sample was dissolved in high-pressure Teflon bombs by an HF-HNO₃ mixture. Rh was used as an internal standard to monitor signal drift during counting in ICP-MS (inductively coupled plasma mass spectrometry) analysis. The USGS rock standard GSP-1 was chosen for calibrating element concentrations of the measured samples, and the certified values of the standard GSP-1 are referred to [25]. Analytical uncertainties for most elements were lower than 5%.

3.3. Trace-Elements and Sr Isotopes in Fluorite

Fluorite separates were obtained by conventional separation techniques and by subsequent handpicking under a binocular microscope (purity >99%); then, they were milled to a 200 mesh for trace and rare earth element analysis. The analyses were performed at Guizhou Tongwei Analytical Technology Co., Ltd. (Gui'an, China) on a ThermoFisher X Series 2 ICP-MS. Powders (approximately 20–30 mg) were digested in double-distilled 6N HCl at 160 °C for 3 days. Sample solutions were diluted to about 3000× with 2% HNO₃ and spiked with Rh, In, Re, and Bi as internal standards. A blank was used to test accuracy. Instrument drift, mass, and matrix bias were corrected with internal spikes and external monitors. The analytical uncertainties are within 3% for most of the elements reported.

The remaining stock solution left from the trace element analyses was used for the separation of Sr by a combination of cation-exchange chromatography in H⁺ form and pyridinium form with the DCTA (diaminocyclohexane tetraacetic acid) complex. The isotope ratios of Sr were analyzed on a Nu Instrument MC-ICP-MS at Guizhou Tongwei Analytical Technology Co., Ltd. The mass fractionation corrections for Sr isotopic ratios were on the basis of ⁸⁶Sr/⁸⁸Sr = 0.1194. Replicate analyses of separate loads of SRM987 yielded a mean ⁸⁷Sr/⁸⁶Sr = 0.710237 ± 0.000027 (2σ). Initial ⁸⁷Sr/⁸⁶Sr ratios were calculated on the basis of muscovite ⁴⁰Ar-³⁹Ar age for the albitized granite (*t* = 145 Ma, [17]).

4. Results

4.1. Trace Elements

The trace elements data for the fluorites and granites are listed in Table 1. Representative trace elements variation diagrams (Mg-Fe, Ti-Mn, Sr-Sc, Cs-Rb, Nb-Ta, Zr-Hf, Th-U and Pb-Zn) for the fluorites are shown in Figure 5.

The albitized granite shows high concentrations of large ion lithophile elements (LILEs) (Rb, 1570 ppm; Cs, 22.4 ppm; Ba, 24.5 ppm; except for Sr, 6.80 ppm) and high field strength elements (HFSEs) (Zr, 40.0 ppm; Hf, 12.1 ppm; Nb, 22.9 ppm; Ta, 29.0 ppm; Th, 12.3 ppm; except for U, 2.44 ppm). In addition, the contents of other elements are as follows: Li (133 ppm), Be (5.06 ppm), Sc (7.80 ppm), Co (0.20 ppm), Ni (0.60 ppm), V (<1 ppm), Cr (7.00 ppm), Cu (14.6 ppm), Zn (275 ppm), Pb (94.8 ppm), Mn (351 ppm), Mo (0.40 ppm), Ga (67.1 ppm), and Sn (32.0 ppm).

The contents of some trace elements in the Type I fluorites are obviously higher than the Type II and III fluorites (Figure 5), such as Fe (197–217 ppm), Sc (2.99–3.20 ppm), Mn (73.8–77.7 ppm), Rb (18.4–20.1 ppm), Zn (8.71–9.37 ppm), Pb (29.5–31.8 ppm), Nb (32.6–52.7 ppm), Ta (7.46–9.25 ppm), Zr (28.1–30.1 ppm), Hf (6.91–7.22 ppm), and Th (14.9–15.2 ppm). The contents of other trace elements in the Type I are similar to those in the Type II and III (Figure 5).

The different-colored fluorites of the Type II show various trace element contents (Figure 5), such as Mg (5.69–24.7 ppm), Fe (49.0–88.8 ppm), and Ti (1.80–18.8 ppm), but they are irregular. Overall, the Type II fluorites show low contents of LILEs (Rb, 0.12–1.05 ppm; Cs, 0.00–0.71 ppm; except for Sr, 105–159 ppm) and HFSEs (Zr, 0.12–0.89 ppm; Hf, <0.03 ppm; Nb, 0.01–0.19 ppm; Ta, <0.01 ppm, Th, 0.02–0.14 ppm and U, 0.04–0.32 ppm).

The Type III fluorites have similar trace element characteristics to the Type II except for lower contents of Sr (76.6–80.5 ppm) (Figure 5).

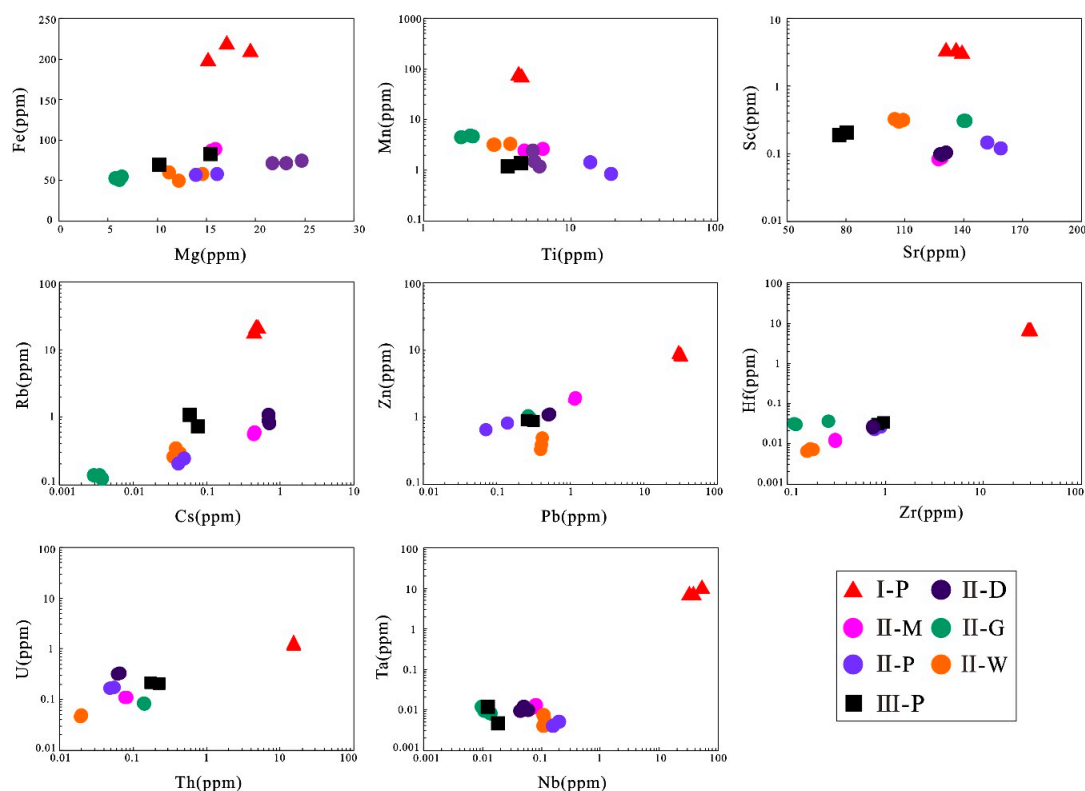


Figure 5. Trace element variation diagrams for fluorites from the Shihuiyao deposit, showing the compositional difference between different types of fluorite.

4.2. REE and Y

The REE and Y data of fluorites and albitized granite are shown in Table 1, and their chondrite-normalized REE patterns are shown in Figure 6.

The albitized granite contains 16 ppm of REE and 1.5 ppm of Y. The chondrite-normalized REE pattern of the granite is characterized by a tetrad effect (Figure 6a), with a strong negative Eu anomaly ($\text{Eu}/\text{Eu}^* = 0.16$) and $(\text{La}/\text{Yb})_N$ value of 0.49.

The Type I fluorites have the highest REE and Y contents of 594–621 and 161–166 ppm, respectively. The REE patterns display tetrad effects, enrichment in HREE, and negative Eu anomaly ($\text{Eu}/\text{Eu}^* = 0.07$), with a low $(\text{La}/\text{Yb})_N$ value of 0.03–0.04 (Figure 6b). In addition, the Type I fluorites have a low Y/Ho value of 8.61–8.76 (Figure 7).

The different-colored fluorites of Type II show a large variation in REE contents, ranging from 2.1 to 74.6 ppm. The II-G fluorites have the highest REE contents of 74.2–74.6 ppm, followed by 6.4 ppm for II-M fluorites, 5.8–6.0 ppm for the II-D fluorites, 4.9–5.3 ppm for the II-P fluorites, and 2.8 ppm for II-W fluorites. The Y concentrations for the different-colored fluorites are 57.4–58.4 ppm for the II-G fluorites, 5.1–5.3 ppm for the II-D fluorites, 3.0 ppm for the II-M fluorites, 2.8 ppm for the II-P fluorites, and 2.1–2.2 ppm for the II-W fluorites. They also show different chondrite-normalized REE patterns (Figure 6c). The II-D fluorites show negative Eu anomalies ($\text{Eu}/\text{Eu}^* = 0.61$ – 0.64), slightly tetrad effects, and low $(\text{La}/\text{Yb})_N$ values of 0.31–0.33 (Figure 6c), while the II-M fluorites show similar Eu/Eu^* (0.58–0.60) and slightly tetrad effects but higher $(\text{La}/\text{Yb})_N$ values (1.08) (Figure 6c). The II-G fluorites also show slightly tetrad effects, with Eu/Eu^* and $(\text{La}/\text{Yb})_N$ values of 0.55–0.58 and 0.54–0.55, respectively (Figure 6c). The II-W fluorites show negligible Eu anomalies ($\text{Eu}/\text{Eu}^* = 0.96$ – 0.98), negative Ce anomalies (average $\text{Ce}/\text{Ce}^* = 0.73$), and the highest $(\text{La}/\text{Yb})_N$ values of 3.23–3.40 (Figure 6c). The II-P fluorites show positive Eu anomalies ($\text{Eu}/\text{Eu}^* = 1.31$ – 1.39), with $(\text{La}/\text{Yb})_N$ values of 0.25–0.36 (Figure 6c). The Type II fluorites show similar Y/Ho ratios except for the II-W fluorites (52.6–54.2), ranging from 22.2 to 29.8 (Figure 7).

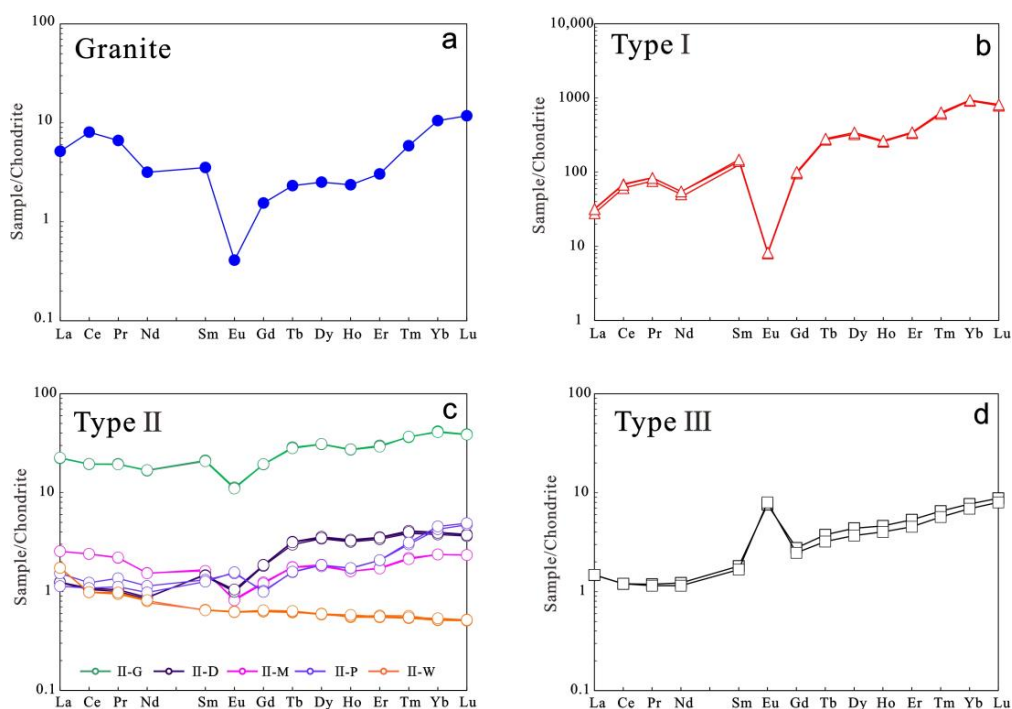


Figure 6. Chondrite-normalized rare earth element (REE) patterns of fluorites from the Shihuiyao deposit (normalized values are from [26]). (a) Chondrite-normalized REE patterns of granite; (b) REE patterns of Type I fluorites; (c) REE patterns of Type II fluorites; (d) REE patterns of Type III fluorites.

The REE and Y concentrations of the Type III fluorites are 8.3–9.1 ppm and 12.5–13.7 ppm, respectively. The REE patterns of the Type III fluorites show HREE enrichment, strongly positive Eu anomalies ($Eu/Eu^* = 3.31\text{--}3.86$), and low $(La/Yb)_N$ values (0.19–0.21) (Figure 6d). The Y/Ho ratios of the Type III fluorites are 41.3–43.4 (Figure 7).

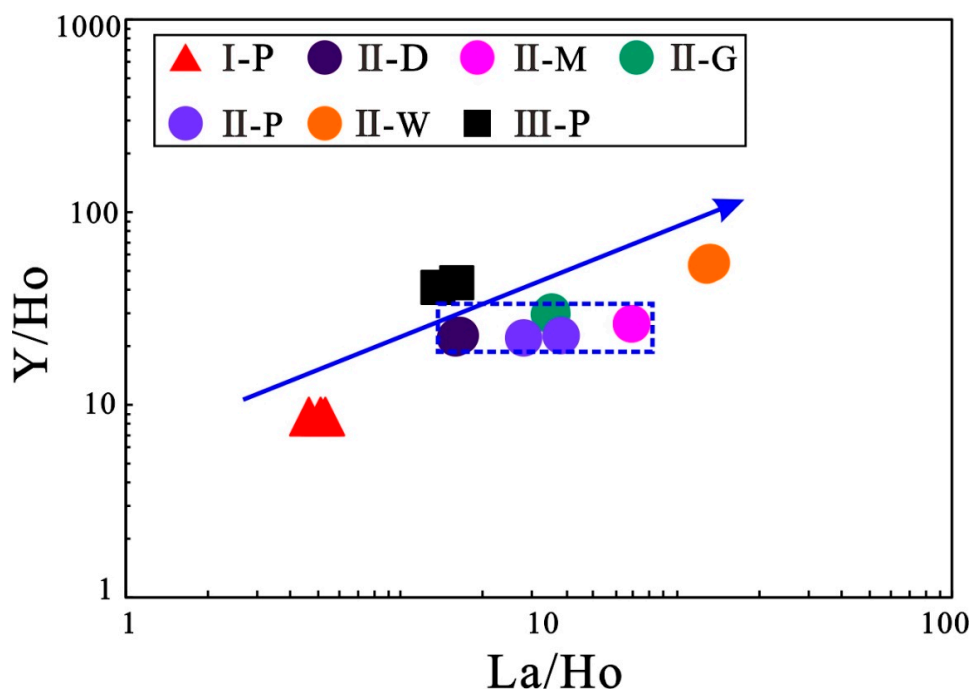


Figure 7. Plot of Y/Ho versus La/Ho for fluorites from the Shihuiyao deposit [27].

Table 1. Trace and rare earth elements data (in ppm) of fluorites and granite from the Shihuiyao deposit.

Type	Granite		Type I			Type II						Type III							
	A-G		I-P		II-D			II-M		II-G		II-P		II-W		III P			
No.	1	1	2	3	1	2	3	1	2	1	2	3	1	2	1	2	3	1	2
Li	133	4.82	4.02	4.17	17.4	16.7	18.4	12.3	11.3	0.04	0.03	0.03	0.63	0.78	0.27	0.25	0.24	0.16	0.26
Be	5.06	0.33	0.18	0.19	0.29	0.30	0.29	0.23	0.18	0.38	0.38	0.38	0.12	0.10	0.63	0.60	0.70	0.14	0.16
Mg	0.01	17.1	19.5	15.2	23.10	21.70	24.70	15.50	15.90	5.69	6.10	6.34	13.90	16.10	12.20	14.60	11.20	10.20	15.40
Sc	7.80	2.99	3.20	3.20	0.09	0.10	0.10	0.08	0.09	0.30	0.31	0.30	0.15	0.12	0.32	0.31	0.30	0.19	0.21
Ti	<0.005	4.42	4.65	4.45	5.63	5.51	6.16	4.86	6.49	2.08	1.80	2.17	13.5	18.8	3.03	3.90	2.98	3.73	4.59
V	<1.00	0.81	0.24	0.23	0.48	0.42	0.48	0.32	0.41	0.05	0.12	0.04	0.36	0.50	0.09	0.12	0.10	0.18	0.23
Cr	7.00	0.08	0.10	0.07	0.31	0.34	0.38	0.27	0.39	0.03	0.02	0.03	0.41	0.56	0.05	0.07	0.06	0.04	0.08
Mn	351	74.5	73.8	77.7	1.47	2.38	1.18	2.40	2.57	4.67	4.44	4.53	1.43	0.82	3.11	3.21	3.14	1.18	1.33
Fe	0.40	217	208	197	71.3	71.2	73.8	86.5	88.8	52.6	49.9	54.2	56.2	57.1	49.0	57.3	59.8	69.0	81.9
Co	0.20	0.02	0.03	0.02	0.02	0.02	0.02	0.02	0.02	0.01	0.01	0.01	0.02	0.02	0.01	0.01	0.01	0.14	0.05
Ni	0.60	0.32	0.30	0.25						0.06	0.04	0.02			0.11	0.13	0.11	0.05	
Cu	14.6	0.49	0.50	0.47	0.10	0.09	0.11	0.12	0.14	0.12	0.10	0.12	0.08	0.07	0.26	0.25	0.23	0.09	0.09
Zn	275	8.90	8.71	9.37	1.05	1.07	1.10	1.78	1.94	0.96	0.86	1.03	0.79	0.63	0.48	0.39	0.33	0.90	0.86
Ga	67.1	4.00	4.28	4.20	0.24	0.22	0.23	0.20	0.22	0.99	0.93	0.97	0.09	0.09	0.08	0.09	0.08	0.11	0.10
Rb	1570	20.1	18.6	18.4	0.87	1.05	0.80	0.54	0.57	0.13	0.12	0.14	0.20	0.24	0.25	0.34	0.28	1.06	0.71
Sr	6.80	139	136	131	129	128	131	127	129	140	141	141	152	159	105	109	107	76.6	80.5
Y	1.50	162.0	166	161	5.3	5.1	5.3	3.0	3.0	57.4	57.5	58.4	2.8	2.8	2.1	2.2	2.2	13.7	12.5
Zr	40.0	30.1	28.1	29.4	0.74	0.74	0.75	0.31	0.31	0.26	0.12	0.12	0.77	0.89	0.17	0.18	0.16	0.82	0.95
Nb	22.9	32.6	38.3	52.7	0.05	0.06	0.04	0.08	0.07	0.01	0.01	0.01	0.16	0.19	0.11	0.12	0.11	0.01	0.02
Mo	0.40	1.94	1.15	2.5	0.54	0.09	1.13	0.06	1.05	1.33	1.07	0.36	0.07	0.74	0.19	0.19	0.29	0.08	0.09
Sn	32.0	11.6	3.62	21.2	2.52	0.87	4.71	0.63	6.21	8.99	5.70	1.05	0.46	3.11	2.67	1.36	1.58	0.61	0.78
Sb	0.07	2.09	3.61	11.2	1.10	0.38	0.50	0.71	2.52	4.80	2.90	0.56	0.39	2.06	3.19	1.39	1.49	0.67	0.36
Cs	22.4	0.47	0.44	0.44	0.70	0.70	0.71	0.44	0.45	0.00	0.00	0.00	0.04	0.05	0.03	0.04	0.04	0.06	0.08
Ba	24.5	3.41	3.23	3.18	6.29	7.26	6.57	4.37	4.52	6.77	6.62	6.51	0.67	0.32	0.50	0.59	0.53	1.54	1.55
La	1.60	8.67	9.83	9.99	0.39	0.38	0.38	0.79	0.79	6.90	6.95	6.97	0.47	0.35	0.54	0.54	0.54	0.46	0.46
Ce	6.50	49.3	54.8	56.1	0.87	0.85	0.80	1.93	1.94	15.7	15.6	15.7	0.99	0.88	0.79	0.80	0.80	0.97	0.97
Pr	0.81	9.25	10.2	10.3	0.13	0.12	0.13	0.27	0.27	2.37	2.36	2.35	0.17	0.14	0.12	0.12	0.12	0.15	0.14
Nd	1.90	30.1	33	32.8	0.52	0.50	0.52	0.92	0.92	10.0	10.1	10.1	0.68	0.59	0.48	0.48	0.49	0.74	0.69
Sm	0.69	27.5	28.8	28.8	0.29	0.28	0.28	0.31	0.31	4.11	4.06	4.05	0.26	0.25	0.13	0.13	0.13	0.35	0.33
Eu	0.03	0.59	0.61	0.59	0.07	0.07	0.08	0.06	0.06	0.83	0.81	0.81	0.11	0.12	0.05	0.05	0.05	0.56	0.59
Gd	0.40	24.9	26	25.1	0.48	0.47	0.48	0.32	0.31	5.00	4.98	5.02	0.26	0.26	0.16	0.16	0.17	0.72	0.64
Tb	0.11	13	13.4	13	0.15	0.14	0.15	0.08	0.08	1.36	1.33	1.33	0.07	0.08	0.03	0.03	0.03	0.18	0.15
Dy	0.81	105	110	105	1.15	1.10	1.12	0.60	0.58	9.96	9.92	9.98	0.60	0.60	0.19	0.19	0.19	1.41	1.19
Ho	0.17	18.5	19.1	18.7	0.24	0.23	0.23	0.12	0.12	1.96	1.94	1.96	0.12	0.12	0.04	0.04	0.04	0.33	0.29

Table 1. Cont.

Type	Granite		Type I			Type II									Type III				
	A-G		I-P		II-D			II-M		II-G			II-P		II-W			III P	
No.	1	1	2	3	1	2	3	1	2	1	2	3	1	2	1	2	3	1	2
Er	0.64	70.5	72.6	70.5	0.74	0.71	0.73	0.36	0.36	6.27	6.14	6.13	0.43	0.44	0.12	0.12	0.12	1.12	0.95
Tm	0.19	19.8	20.7	19.8	0.13	0.13	0.13	0.07	0.07	1.18	1.19	1.19	0.10	0.10	0.02	0.02	0.02	0.21	0.18
Yb	2.20	191	196	192	0.83	0.79	0.82	0.49	0.49	8.67	8.57	8.54	0.89	0.95	0.11	0.11	0.11	1.61	1.44
Lu	0.38	25.4	26.3	25.4	0.12	0.12	0.12	0.08	0.08	1.25	1.25	1.24	0.15	0.16	0.02	0.02	0.02	0.28	0.26
Hf	12.1	7.22	6.91	7.1	0.03	0.02	0.02	0.01	0.01	0.03	0.03	0.03	0.02	0.02	0.01	0.01	0.01	0.03	0.03
Ta	29.0	7.5	7.46	9.25	0.01	0.01	0.01	0.01	0.01	0.01	0.01	0.01	0.00	0.00	0.00	0.01	0.01	0.01	0.00
Pb	94.8	30.7	31.8	29.5	0.51	0.52	0.54	1.17	1.18	0.29	0.28	0.27	0.14	0.07	0.43	0.41	0.40	0.26	0.32
Th	12.3	15.2	15.2	14.9	0.07	0.06	0.07	0.08	0.08	0.14	0.14	0.14	0.06	0.05	0.02	0.02	0.02	0.22	0.17
U	2.44	1.39	1.27	1.32	0.32	0.31	0.32	0.11	0.11	0.08	0.08	0.08	0.17	0.16	0.04	0.05	0.05	0.20	0.21

4.3. Fluorite Sr Isotopic Compositions

The Sr isotopic compositions of fluorites are listed in Table 2. As shown in Figure 8, the $(^{87}\text{Sr}/^{86}\text{Sr})_i$ ratios of different types of fluorites are rather variable. The Type I fluorites have relatively high $(^{87}\text{Sr}/^{86}\text{Sr})_i$ ratios of 0.710861. For the Type II fluorites, the II-W fluorites have slightly high $(^{87}\text{Sr}/^{86}\text{Sr})_i$ ratios of 0.710378–0.710380, and the other colored fluorites have similar $(^{87}\text{Sr}/^{86}\text{Sr})_i$ ratios, ranging from 0.710168 to 0.710197 (average 0.710182). The Type III fluorites have lower $(^{87}\text{Sr}/^{86}\text{Sr})_i$ ratios of 0.709018.

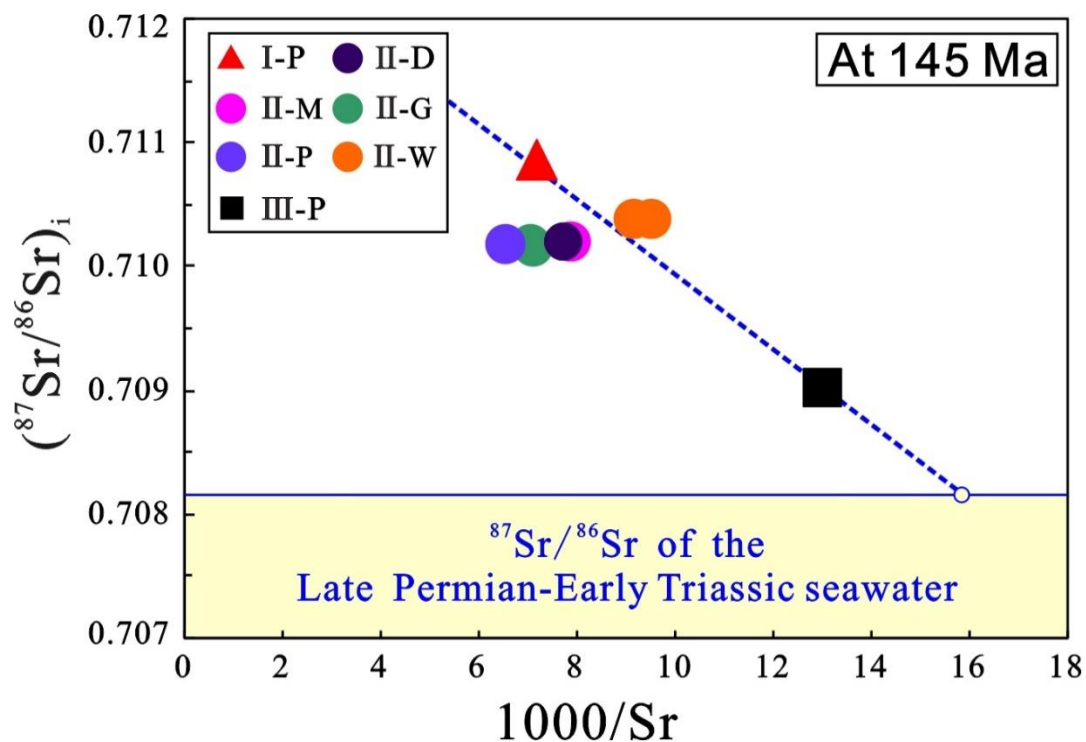


Figure 8. Plot of $(^{87}\text{Sr}/^{86}\text{Sr})_i$ ratio versus $1000/\text{Sr}$ for fluorites from the Shihuiyao deposit. All isotopic data are corrected at 145 Ma [17]. The Sr isotope data of the Late Permian–Early Triassic seawater are from [28].

Table 2. Sr isotopic compositions of fluorites from the Shihuiyao deposit.

Type	Type I			Type II			Type III	
	I-P	II-D	II-M	II-G	II-P	II-W		III-P
No.	1	1	1	1	1	1	2	1
Rb ^a (ppm)	20.1	0.87	0.54	0.12	0.20	0.25	0.34	1.06
Sr ^a (ppm)	139	129	127	141	152	105	109	76.6
⁸⁷ Rb/ ⁸⁶ Sr	0.4188	0.0195	0.0124	0.0025	0.0039	0.0069	0.0090	0.0401
⁸⁷ Sr/ ⁸⁶ Sr ± 2σ	0.711708 ± 6	0.710237 ± 6	0.710212 ± 7	0.710181 ± 5	0.710175 ± 6	0.710392 ± 7	0.710398 ± 7	0.709099 ± 5
(⁸⁷ Sr/ ⁸⁶ Sr) _i ^b	0.710861	0.710197	0.710187	0.710176	0.710168	0.710378	0.710380	0.709018

^a Contents determined by ICP-MS (values from Table 1). ^b Recalculation of (⁸⁷Sr/⁸⁶Sr)_i to 145 Ma [17] using λ⁸⁷Rb = 1.393 × 10⁻¹¹ year⁻¹ [29].

5. Discussion

5.1. Origin of Fluorite Formation

5.1.1. Type I Fluorites

The total REE concentration in hydrothermal fluids is controlled by pH and the bulk chemical composition of the hydrothermal fluid [30]. Generally, REE concentrations increase with decreasing pH. In acidic solutions with low concentrations of complexing ligands, the LREE (light rare earth element) are enriched with respect to the HREE (heavy rare earth element), which are preferentially adsorbed onto the surface [31]. In alkaline fluids with mono- and bicarbonate species and/or halogens as complexing ligands, the HREE-enriched patterns displayed as HREE are more strongly complexed than LREE [31–34]. From this point of view, the fluids where the Type I fluorites precipitated were alkaline and HREE-enriched. According to Möller [35], an enrichment of HREE in fluorites would indicate a Ca^{2+}/F ratio < 1 in parent fluids. This means that the fluids originated from an F-rich source or the mobilization of pre-existing fluorite mineralization in deeper parts of the crust [36]. This interpretation may apply to the Type I fluorites. Similar to the albitized granite, the Type I fluorites have relatively high Rb and HFSEs contents (Figure 5) and display strong negative Eu anomalies and tetrad effects (Figure 6a,b). Moreover, the greisen pockets are texturally isolated bodies occurring within the albitized granite, with no evidence that they are connected with each other. Hence, in summary, we suggest that the Type I fluorites from the greisen are related to the immiscible aqueous F-rich fluids formed in the late stage of the granite crystallization, which is similar to many greisen pockets observed elsewhere [37–39]. All the components of the Type I fluorites are derived from albitized granites.

5.1.2. Type II Fluorites

The Type II fluorites show various REE patterns (Figure 6c) and La/Ho ratios (Figure 7). There are two hypotheses to explain these phenomena: (1) mineral paragenesis; (2) fluid-rock interaction.

Mineral paragenesis may significantly affect the REE patterns of fluorite, as the REE can also enter other minerals. The minerals accompanied by fluorites are chalcedony and some calcites. Chalcedony cannot compete with fluorite for the uptake of the REE, and carbonates generally precipitated later than fluorites in the Shihuiyao mineralization. Thus, their crystallization has no effect on the REE contents of the fluorites. As a whole, the mineral paragenesis did not control the REE patterns of the Type II fluorites.

Therefore, various REE patterns and La/Ho ratios of the Type II fluorites are due to the interaction between fluids and wall rocks (marine limestones), which is in agreement with field evidence that skarn is the host rock of the Type II fluorites. Bau and Dulski [27] proposed that the Y/Ho ratios will increase during the migration of F-rich fluids. Hence, in the Type II fluorites, the subtype II-D, II-M, II-G, and II-P fluorites should crystallize later than the Type I fluorites, followed by the subtype II-W fluorites (Figure 7). Similar to the Type I fluorites, the II-D, II-M and II-G fluorites show negative Eu anomalies and slightly tetrad effects (Figure 6c), and the II-P fluorites also display slight tetrad effects (Figure 6c). Hence, these fluorites may form by the mixing of magmatic and limestone components in the early hydrothermal stage, and then, the II-W fluorites may form in the late-hydrothermal stage. The granite-derived fluids provide F for the Type II fluorites, while the limestone components are the main Ca source. The REE, especially HREE, which are more strongly complexed than LREE [32–34], were removed by early crystalline fluorites; thus, the II-W fluorites display HREE-depletion patterns.

5.1.3. Type III fluorites

The Y/Ho ratios of the Type III fluorites are lower than the type II-W fluorites but higher than the other colored fluorites of Type II (Figure 7), suggesting that the formation of the Type III fluorites may be between the II-W fluorites and other Type II fluorites.

Considering the interaction between fluids and the host rocks, according to Schwinn and Markle [31], REE patterns of fluorite similar to those of the host rock may mean that the host rock is the source of REE. The REE contents of aluminosilicate rocks may be several orders of magnitude higher than those of marine limestones [40], and the chondrite-normalized REE patterns generally exhibit LREE-enrichment and negative Eu anomalies [41–45]. In contrast, the Type III fluorites show quite different REE patterns (Figure 6d). This would suggest that the host rock, i.e., silty mudstones, is not the source of the REE of the Type III fluorites. Therefore, the contributions from silty mudstones in the fluids where the Type III fluorites precipitated may be negligible.

The trace elements contents (except for Sr) of the Type III fluorites are similar to the Type II (Figure 5). Thus, we suggest that the Type III fluorites likely have the same origin as the Type II, i.e., mixing of granite-derived fluids and limestones (see the discussion above). Fluorine comes from granite-derived fluids, while Ca comes from limestones. The early crystallization of albite in veins would remove LREE and some Sr, further leading to the LREE depletion and low Sr contents of the Type III fluorites.

5.2. Fluid Condition

Generally, the $\text{Eu}^{3+}/\text{Eu}^{2+}$ redox potential of hydrothermal fluids depends strongly on temperature and slightly on pH, and it is almost unaffected by pressure [46]. Thermochemical reduction of Eu^{3+} to Eu^{2+} can occur at high temperature ($>200\text{ }^{\circ}\text{C}$); therefore, hydrothermal fluorite will show the Eu anomaly of the fluid only when it crystallizes below $200\text{ }^{\circ}\text{C}$ [31]. At $T > 200\text{ }^{\circ}\text{C}$, the size of Eu^{2+} prevents its substitution for Ca^{2+} in the fluorite structure, and the mineral exhibits a negative Eu anomaly, whereas the fluorite deposited by such a fluid will show no or a slightly positive Eu anomaly at $T < 200\text{ }^{\circ}\text{C}$ [47,48]. In view of this, the decrease of temperature during fluid migration may be responsible for the various Eu anomalies of the Type II fluorites (except for the II-W).

Oxygen fugacity may also affect the presence of the Eu anomaly. In an oxidizing environment, Eu^{2+} is oxidized to Eu^{3+} , which more readily enters the fluorite lattice. Hence, during fluid migration, the increase of fluid oxygen fugacity may lead to the transition of Eu from negative to positive anomalies in the Type II fluorites (except for the II-W). In such an environment, Ce^{3+} is also oxidized to Ce^{4+} , which becomes immobile, or very mobile if it is strongly complexed [49]. The later fluid would become Ce depleted; thus, the II-W fluorites that formed in the late-hydrothermal stage show negative Ce anomalies (average $\text{Ce}/\text{Ce}^* = 0.73$) (Figure 6c).

The Type III fluorites show more pronounced positive Eu anomalies (Figure 6d). The host rocks provided negligible contributions (see the discussion above), and temperature reduction is not enough to cause these anomalies. Hence, we suggest that as well as the decrease of temperature, a more oxidizing environment may account for the formation of the Type III fluorites.

5.3. Source of Sr

The Type I fluorites are related to the immiscible F-rich fluids formed in the late stage of the granite crystallization (see the discussion above); therefore, it is suggested that the Sr isotopic compositions ($(^{87}\text{Sr}/^{86}\text{Sr})_i = 0.710861$) of the Type I fluorites can represent those of the granite-derived fluids.

The $(^{87}\text{Sr}/^{86}\text{Sr})_i$ ratios (0.710168–0.710380) of the Type II fluorites are lower than the $(^{87}\text{Sr}/^{86}\text{Sr})_i$ ratio of the granite-derived fluids (0.710861) but higher than the $^{87}\text{Sr}/^{86}\text{Sr}$ ratios of the Late Permian–Early Triassic seawater (0.7070–0.7082) [28] (Figure 8). It could be explained by precipitation from a fluid with a mixed Sr-source, including the granite-derived fluids and limestones, which is in agreement with the origin of the Type II fluorites (see the discussion above).

Compared to the Type II fluorites, the Type III fluorites show a lower $(^{87}\text{Sr}/^{86}\text{Sr})_i$ ratio (0.709018) (Figure 8). Based on the petrography, two hypotheses are suggested here to explain this phenomenon: (1) the contribution of the silty mudstones and (2) mixing of a larger proportion of limestones than the Type II fluorites. As discussed above, we suggested that there were neglected contributions from silty mudstones in the fluid where the Type III fluorites precipitated. Moreover, the aluminosilicate rocks

generally have much higher $^{87}\text{Sr}/^{86}\text{Sr}$ ratios than marine limestones [46,50], suggesting that the silty mudstones are unlikely the Sr source of the Type III fluorites. Thus, a binary mixed process between an F-rich end member with a high $^{87}\text{Sr}/^{86}\text{Sr}$ ratio (i.e., F-rich fluid exsolved from granite) and a second end member containing a lower Sr isotope ratio (i.e., marine limestones) is also suitable to explain the Sr source of the Type III fluorites. However, the proportion of limestones in the mixture forming the Type III fluorites is much higher than that of the Type II, so as to produce such low Sr isotopic compositions.

5.4. Implication for the Nb-Ta Mineralization

Generally, Nb and Ta are difficult to enter the fluid phase during the magmatic-hydrothermal evolution because of the low fluid/melt partition coefficients ($D_{\text{Nb}}^{\text{fluid-melt}} = 0-0.1$; $D_{\text{Ta}}^{\text{fluid-melt}} = 0.002-0.08$) [51,52]. However, some studies reported that the solubility of Nb and Ta in the fluid can increase with the increase of F contents [53–56].

In the Shihuiyao mining area, the greisen pockets where the Type I fluorites precipitated were formed by the immiscible F-rich fluids exsolved in the late-magmatic stage (see the discussion above). During fluids exsolution, Nb and Ta would form strong complexes with F and migrate into the fluid. When the volatiles and Nb-Ta were enriched to a certain extent, mica and Type I fluorite began to crystallize, resulting in a significant decrease in F in the fluid, which led to the crystallization of Nb-Ta minerals [57–60]. This metallogenic model can also prove why Nb-Ta mineralization is closely related to the greisenization of granite [18].

During the magmatic stage, most of the Nb and Ta were removed with the precipitation of Nb-Ta minerals (mainly columbite-group minerals). As a result, the fluids that evolved in the subsequent lower-temperature hydrothermal stage had no or little Nb and Ta. Thus, Nb-Ta mineralization did not occur in the skarn zone or veins in the silty mudstone where the Type II and III fluorites formed, respectively.

6. Conclusions

(1) In the Shihuiyao Nb-Ta-Rb rare metal mining area, three types of fluorites are found occurring in greisen pockets of the albitized granite (Type I), the skarn zone between the albitized granite and wall rocks (Type II), and fluorite-bearing veins in silty mudstones (Type III).

(2) The Type I fluorites are related to the immiscible F-rich fluids exsolved in the late-magmatic stage. The Type II and III fluorites formed from the early- or late-hydrothermal fluids, which have a mixed signature of the granite-derived fluids and limestones.

(3) As fluid cooling and oxygen fugacity increased, the Type II fluorites display various Eu and Ce anomalies, and the Type III fluorites that formed in a more oxidizing environment show the strongest positive Eu anomalies.

(4) The Type I fluorites have a Sr source derived from granite, whereas the Type II and III fluorites have the same binary mixed Sr sources, i.e., the granite-derived fluids and marine limestones. However, the proportion of limestone components in the Type III fluorites is much higher than that of Type II.

(5) Nb and Ta get into the F-rich fluids by F-Nb (Ta) complexes and precipitate in the form of columbite-group minerals after the Type I fluorites precipitate. As a result, there is no Nb-Ta mineralization in the subsequent hydrothermal stage when the Type II and III fluorites crystallize.

Author Contributions: Field work, Z.-P.D., S.-Y.J., H.-M.S., X.-Y.Z., X.-Y.C., and T.Z.; experiment, Z.-P.D., and T.Z.; data analysis, Z.-P.D., H.-M.S., and X.-Y.C.; writing—original draft preparation, Z.-P.D., T.Z., X.-Y.C., X.-Y.Z., and H.-M.S.; writing—revision and editing, S.-Y.J. All authors have read and agreed to the published version of the manuscript.

Funding: This study was financially supported by projects from the National Key R&D Program of China (No. 2017YFC0602403&05) and Program of the China Geological Survey (No. DD20160072).

Acknowledgments: We would like to thank Shen Nengping for his help with lab work. Four anonymous reviewers provided very helpful suggestions that significantly improved this manuscript.

Conflicts of Interest: The authors declare no conflict of interest.

References

1. Sasmaz, A.; Yavuz, F.; Sağiroğlu, A.; Akgül, B. Geochemical patterns of the Akdağmadeni (Yozgat, Central Turkey) fluorite deposits and implications. *J. Asian Earth Sci.* **2005**, *24*, 469–479. [[CrossRef](#)]
2. Sasmaz, A.; Önal, A.; Sağiroğlu, A.; Önal, M.; Akgül, B. Origin and nature of the mineralizing fluids of thrust zone fluorites in Celikhan (Adiyaman, Eastern Turkey): A geochemical approach. *Geochem. J.* **2005**, *39*, 131–139. [[CrossRef](#)]
3. Sasmaz, A.; Yavuz, F. REE geochemistry and fluid inclusion studies of fluorite deposits from the Yaylagzü area (Yıldızeli-Sivas) in central Turkey. *Neues Jahrb. Geol. Palaontol. Abh.* **2007**, *183*, 215–226.
4. Dill, H.G.; Hansen, B.T.; Weber, B. REE contents, REE minerals and Sm/Nd isotopes of granite- and unconformity-related fluorite mineralization at the western edge of the Bohemian massif: With special reference to the Nabburg-Wölsendorf District, SE Germany. *Ore Geol. Rev.* **2011**, *40*, 132–148. [[CrossRef](#)]
5. Souissi, F.; Souissi, R.; Dandurand, J.L. The Mississippi valley type (MVT) fluorite ore at Jebel Stah (Zaghuan District, northeastern Tunisia): Contribution of REE and Sr isotope geochemistries to the genetic model. *Ore Geol. Rev.* **2010**, *37*, 15–30. [[CrossRef](#)]
6. Ehya, F. Variation of mineralizing fluids and fractionation of REE during the emplacement of the vein-type fluorite deposit at Bozijan, Markazi Province, Iran. *J. Geochem. Explor.* **2012**, *112*, 93–106. [[CrossRef](#)]
7. Akgul, B. Geochemical associations between fluorite mineralization and A-type shoshonitic magmatism in the Keban-Elazig area, East Anatolia, Turkey. *J. Afr. Earth Sci.* **2015**, *111*, 222–230. [[CrossRef](#)]
8. Azizi, M.R.; Abedini, A.; Alipour, S.; Niroomand, S.; Sasmaz, A.; Talaei, B. Rare earth element geochemistry and tetrad effect in fluorites: A case study from the QahrAbad deposit, Iran. *Neues Jahrb. Geol. Palaontol. Abh.* **2017**, *283*, 255–273. [[CrossRef](#)]
9. Pei, Q.; Zhang, S.T.; Santosh, M.; Cao, H.W.; Zhang, W.; Hu, X.K.; Wang, L. Geochronology, geochemistry, fluid inclusion and C, O and Hf isotope compositions of the Shuitou fluorite deposit, Inner Mongolia, China. *Ore Geol. Rev.* **2017**, *83*, 174–190. [[CrossRef](#)]
10. Jiang, Y.H.; Ling, H.F.; Jiang, S.Y.; Shen, W.Z.; Fan, H.H.; Ni, P. Trace element and Sr-Nd isotope geochemistry of fluorite from the Xiangshan uranium deposit southeast China. *Econ. Geol.* **2006**, *101*, 1613–1622. [[CrossRef](#)]
11. Uras, Y.; Nikiforov, A.V.; Oner, F.; Parlak, O. Geochemistry and Nd, Sr Isotopes of the Pohrenk Fluorites (Kirsehir-Turkey). *Geochem. Int.* **2017**, *55*, 263–281. [[CrossRef](#)]
12. Sallet, R.; Moritz, R.; Fontiginie, D. Fluorite $^{87}\text{Sr}/^{86}\text{Sr}$ and REE constraints on fluid-melt relations, crystallization time span and DSr of evolved high-silica granites, Tabuleiro granites, Santa Catarina, Brazil. *Chem. Geol.* **2000**, *164*, 81–92. [[CrossRef](#)]
13. Sallet, R.; Moritz, R.; Fontiginie, D. The use of vein fluorite as probe for paleofluid REE and Sr-Nd isotope geochemistry: The Santa Catarina Fluorite District, Southern Brazil. *Chem. Geol.* **2005**, *223*, 227–248. [[CrossRef](#)]
14. Sánchez, V.; Cardellach, E.; Corbella, M.; Vindel, E.; Martín-Crespo, T.; Boyce, A.J. Variability in fluid sources in the fluorite deposits from Asturias (N Spain): Further evidences from REE, radiogenic (Sr, Sm, Nd) and stable (S, C, O) isotope data. *Ore Geol. Rev.* **2010**, *37*, 87–100. [[CrossRef](#)]
15. Liu, S.; Fan, H.R.; Yang, K.F.; Hu, F.F.; Wang, K.Y.; Chen, P.K.; Yang, Y.H.; Yang, Z.F.; Wang, Q.W. Mesoproterozoic and Paleozoic hydrothermal metasomatism in the giant Bayan Obo REE-Nb-Fe deposit: Constrains from trace elements and Sr-Nd isotope of fluorite and preliminary thermodynamic calculation. *Precambrian Res.* **2018**, *311*, 228–246. [[CrossRef](#)]
16. Zhu, J.Z.; Lu, X.C.; Yao, Z.W. Geological characteristics and metallogenic regularity of rare metal deposit in Shihuiyao, Inner Mongolia. *Miner. Explor.* **2013**, *4*, 635–641.
17. Sun, Y.; Wang, R.J.; Li, J.K.; Zhao, Z. ^{40}Ar - ^{39}Ar dating of the muscovite and regional exploration prospect of Shihuiyao rubidium-multi-metal deposit, Selenhot, Inner Mongolia. *Geol. Rev.* **2015**, *61*, 463–468, (In Chinese with English Abstract).
18. Duan, X.Z.; Shi, H.; Tan, K.X.; Xie, Y.S.; Chen, L.; Han, S.L.; Hu, Y.; Feng, Z.G.; Zhang, Y.Q.; Guo, H.F.; et al. Geology and genesis of the granitic niobium-tantalum-rubidium deposit in Shihuiyao area, Inner Mongolia. *Geol. Resour.* **2016**, *25*, 32–40. (In Chinese)
19. Liu, Y.J.; Li, W.; Feng, Z.P.; Wen, Q.B.; Neubauer, F.; Liang, C.Y. A review of the Paleozoic tectonics in the eastern part of Central Asian Orogenic Belt. *Gondwana Res.* **2017**, *43*, 123–148. [[CrossRef](#)]

20. Mao, J.W.; Xie, G.Q.; Zhang, Z.H.; Li, X.F.; Wang, Y.T.; Zhang, C.Q.; Li, Y.F. Mesozoic large-scale metallogenic pulses in North China and corresponding geodynamic settings. *Acta Petrol. Sin.* **2005**, *21*, 169–188.
21. Wu, F.Y.; Sun, D.Y.; Ge, W.C.; Zhang, Y.B.; Grant, M.L.; Wilde, S.A.; Jahn, B.M. Geochronology of the Phanerozoic granitoids in northeastern China. *J. Asian Earth Sci.* **2011**, *41*, 1–30. [[CrossRef](#)]
22. Han, J.; Zhou, J.B.; Wang, B.; Cao, J.L. The final collision of the CAOB: Constraint from the zircon U-Pb dating of the Linxi Formation, Inner Mongolia. *Geosci. Front.* **2015**, *6*, 211–225. [[CrossRef](#)]
23. Zhai, D.X.; Zhang, Y.S.; Tian, S.G.; Wu, F.M.; Xing, E.Y.; Wang, M.; Shi, L.Z.; Wang, Z.Z. Sedimentary environment and evolution of the Upper Permian Linxi Formation in Linxi area, Inner Mongolia. *J. Palaeogeogr.* **2015**, *17*, 359–370. (In Chinese)
24. Gao, J.F.; Lu, J.J.; Lai, M.Y.; Lin, Y.P.; Pu, W. Analysis of trace elements in rock samples using HR-ICPMS. *J. Nanjing Univ. (Nat. Sci.)* **2003**, *39*, 844–850. (In Chinese)
25. Govindaraju, K. Compilation of working values and sample description for 383 geostandards. *Geostandards Newsletter* **1994**, *18*, 1–158. [[CrossRef](#)]
26. Boynton, W.V. Geochemistry of the rare earth elements: Meteorite studies. In *Rare Earth Element Geochemistry*; Henderson, P., Ed.; Elsevier: New York, NY, USA, 1984.
27. Bau, M.; Dulski, P. Comparative study of yttrium and rare-earth element behaviours in fluorine-rich hydrothermal fluids. *Contrib. Mineral. Petrol.* **1995**, *119*, 213–223. [[CrossRef](#)]
28. Korte, C.; Kozur, H.W.; Bruchsch, P.; Veizer, J. Strontium isotope evolution of Late Permian and Triassic seawater. *Geochim. Cosmochim. Acta* **2003**, *67*, 47–62. [[CrossRef](#)]
29. Nebel, O.; Scherer, E.E.; Mezger, K. Evaluation of the ^{87}Rb decay constant by age comparison against the U-Pb system. *Earth Planet. Sci. Lett.* **2011**, *301*, 1–8. [[CrossRef](#)]
30. Michard, A. Rare earth element systematics in hydrothermal fluids. *Geochim. Cosmochim. Acta* **1989**, *53*, 745–750. [[CrossRef](#)]
31. Schwinn, G.; Markl, G. REE systematics in hydrothermal fluorite. *Chem. Geol.* **2005**, *216*, 225–248. [[CrossRef](#)]
32. Wood, S.A. The aqueous geochemistry of the rare earth elements and yttrium. Review of available low temperature data for inorganic complexes and the inorganic REE speciation of natural waters. *Chem. Geol.* **1990**, *82*, 159–186. [[CrossRef](#)]
33. Wood, S.A. The aqueous geochemistry of the rare earth elements and yttrium. Theoretical predictions of speciation in hydrothermal solutions to 350 °C at saturation water vapor pressure. *Chem. Geol.* **1990**, *88*, 99–125. [[CrossRef](#)]
34. Haas, J.R.; Shock, E.L.; Sassani, D. Rare earth in hydrothermal systems: Estimates of standard partial molal thermodynamic of aqueous complexes of rare earth elements at high pressures and temperatures. *Geochim. Cosmochim. Acta* **1995**, *21*, 4329–4350. [[CrossRef](#)]
35. Möller, P. REE fractionation in hydrothermal fluorite and calcite. In *Source, Transport and Deposition of Metals*; Pagel, M., Leroy, J., Eds.; Balkema: Rotterdam, The Netherlands, 1991; pp. 91–94.
36. Lüders, V. Formation of hydrothermal fluorite deposits of the Harz Mountains, Germany. In *Source, Transport and Deposition of Metals*; Pagel, M., Leroy, J.L., Eds.; Balkema: Rotterdam, The Netherlands, 1991; pp. 325–328.
37. Borges, R.M.K.; Villas, R.N.N.; Fuzikawa, K.; Dall’Agnol, R.; Pimenta, M.A. Phase separation, fluid mixing, and origin of the greisens and potassic episyenite associated with the gua boa pluton, pitinga tin province, amazonian craton, Brazil. *J. S. Am. Earth Sci.* **2009**, *27*, 161–183. [[CrossRef](#)]
38. Zhu, X.Y.; Wang, J.B.; Wang, Y.L.; Cheng, X.Y.; He, P.; Fu, Q.B.; Li, S.T. Characteristics of greisen inclusions in alkali feldspar granite of Yaogangxian tungsten deposit. *Miner. Depos.* **2013**, *32*, 533–544. (In Chinese)
39. Dong, Y.C. Characteristics of greisenization of granite-type W-Sn deposit in Limu of Guangxi. *Miner. Resour. Geol.* **2014**, *28*, 699–706. (In Chinese)
40. Parekh, P.P.; Möller, P.; Dulski, P. Distribution of trace elements between carbonate and non-carbonate phases of limestones. *Earth Planet. Sci. Lett.* **1977**, *34*, 39–50. [[CrossRef](#)]
41. Denis, E.; Dabard, M.P. Sandstone petrography and geochemistry of late proterozoic sediments of the armorican massif (France)-A key to basin development during the cadomian orogeny. *Precambrian Res.* **1989**, *42*, 189–206. [[CrossRef](#)]
42. Maravelis, A.; Zelilidis, A. Petrography and geochemistry of the late Eocene-early Oligocene submarine fans and shelf deposits on Lemnos Island, NE Greece. Implications for provenance and tectonic setting. *Geol. J.* **2010**, *45*, 412–433. [[CrossRef](#)]

43. Ghosh, S.; Sarkar, S. Geochemistry of Permo-Triassic mudstone of the Satpura Gondwana basin, central India: Clues for provenance. *Chem. Geol.* **2010**, *277*, 78–100. [[CrossRef](#)]
44. Xie, Q.F.; Zhou, L.F.; Cai, Y.F.; Liu, Y.; Liu, Z.W. Geochemistry and Geological Significance of the Permian Mudstone in the South Qilian Basin China. *Bull. Miner. Petrol. Geochem.* **2015**, *34*, 354–361.
45. Li, F.L.; Xiao, F.; Meng, F.C.; Ren, Z.Y. Geochemical characteristics and implication for provenance of Upper Permian Linxi Formation clastic rocks in Solonker area, Inner Mongolia. *J. Jilin Univ. (Earth Sci. Ed.)* **2016**, *46*, 1769–1780. (In Chinese)
46. Castorina, F.; Masi, U.; Padalino, G.; Palomba, M. Trace-element and Sr-Nd isotopic evidence for the origin of the Sardinian fluorite mineralization (Italy). *Appl. Geochem.* **2008**, *23*, 2906–2921. [[CrossRef](#)]
47. Bau, M. Rare-earth element mobility during hydrothermal and metamorphic fluid-rock interaction and the significance of the oxidation state of europium. *Chem. Geol.* **1991**, *93*, 219–230. [[CrossRef](#)]
48. Möller, P.; Holzbecher, E. Eu anomalies in hydrothermal fluids and minerals: A combined thermochemical and dynamic phenomenon. *Freib. Forsch.* **1998**, *475*, 73–84.
49. Möller, P.; Bau, M.; Dulski, P.; Lüders, V. REE and Y fractionation in fluorite and their bearing on fluorite formation. In Proceedings of the Ninth Quadrennial IAGOD Symposium, Beijing, China, 12–18 August 1994; pp. 575–592.
50. Simonetti, A.; Bell, K. Nd, Pb, and Sr systematics of fluorite at the Amba Donger carbonatite complex, India: Evidence for hydrothermal and crustal fluid mixing. *Econ. Geol.* **1995**, *90*, 2018–2027. [[CrossRef](#)]
51. London, D.; Hervig, R.L.; Morgan, G.B. Melt-vapor solubilities and elemental partitioning in peraluminous granite-pegmatite systems: Experimental results with Macusani glass at 200 MPa. *Contrib. Mineral. Petrol.* **1988**, *99*, 360–373. [[CrossRef](#)]
52. Zaraisky, G.P.; Korzhinskaya, V.; Kotova, N. Experimental studies of Ta₂O₅ and columbite-tantalite solubility in fluoride solutions from 300 to 550 °C and 50 to 100 MPa. *Mineral. Petrol.* **2010**, *99*, 287–300. [[CrossRef](#)]
53. Keppler, H. Influence of fluorine on the enrichment of high field strength trace elements in granitic rocks. *Contrib. Mineral. Petrol.* **1993**, *114*, 479–488. [[CrossRef](#)]
54. Badanina, E.V.; Syritso, L.F.; Volkova, E.V.; Thomas, R.; Trumbull, R.B. Composition of Li-F granite melt and its evolution during the formation of the ore-bearing Orlovka Massif in Eastern Transbaikalia. *Petrology* **2010**, *18*, 131–157. [[CrossRef](#)]
55. Timofeev, A.; Williams-Jones, A.E. The Origin of Niobium and Tantalum Mineralization in the Nechalacho REE Deposit, NWT, Canada. *Econ. Geol.* **2015**, *110*, 1719–1735. [[CrossRef](#)]
56. Timofeev, A.; Migdisov, A.A.; Williams-Jones, A.E. An experimental study of the solubility and speciation of tantalum in fluoride-bearing aqueous solutions at elevated temperature. *Geochem. Cosmochim. Acta* **2017**, *197*, 294–304. [[CrossRef](#)]
57. Linnen, R.L.; Samson, I.M.; Williams-Jones, A.E. Geochemistry of the rare-earth element, Nb, Ta, Hf, and Zr deposits. *Geology* **2014**, *13*, 543–564.
58. Bartels, A.; Vetere, F.; Holtz, F.; Behrens, H.; Linnen, R.L. Viscosity of flux-rich pegmatitic melts. *Contrib. Mineral. Petrol.* **2011**, *162*, 60–61. [[CrossRef](#)]
59. Linnen, R.L.; Keppler, H. Columbite solubility in granitic melts; consequences for the enrichment and fractionation of Nb and Ta in the Earth's crust. *Contrib. Mineral. Petrol.* **1997**, *128*, 213–227. [[CrossRef](#)]
60. Linnen, R.L.; Cuney, M. Granite-related rare-element deposits and experimental constraints on Ta-Nb-W-Sn-Zr-Hf mineralization. In *Rare Element Geochemistry and Mineral Deposits*; Linnen, R.L., Samson, I.M., Eds.; Geological Association of Canada: St. John's, NL, Canada, 2005; pp. 45–68.

